Beryllium-10 concentrations in the hyper-arid soils in the Atacama Desert, Chile: Implications for arid soil formation rates and El Niño driven changes in Pliocene precipitation

Fan Wang [a], Greg Michalski [a,b,*], Ji-Hye Seo [b], Darryl E. Granger [a], Nathaniel Lifton [a,c], Marc Caffee [a,c]

[a] *Department of Earth, Atmospheric and Planetary Sciences, Purdue University, West Lafayette, IN 47907, USA*
[b] *Department of Chemistry, Purdue University, West Lafayette, IN 47907, USA*
[c] *Department of Physics and Astronomy, Purdue University, West Lafayette, IN 47907, USA*

Abstract

Meteoric ^{10}Be concentrations in soil were measured to understand the mechanism, timescale, and climatic dependence of soil formation in the hyper-arid Atacama Desert. The observed systematic decline of soil ^{10}Be concentrations with depth has been reproduced using a simple model that assumes soil matrix, including ^{10}Be, builds up as layers over time while ^{10}Be decays *in situ*. This suggests a mechanism of soil accumulation via atmospheric deposition, which is in agreement with stable isotopic evidence. The model estimates an age of $\sim 6.6 \pm 0.4$ Ma for the total soil profile. Small discrepancies between the model and observations are likely mainly due to changes in precipitation rates that can impact ^{10}Be delivery rates and ^{10}Be movement within the profile. Interpreted in this way, the ^{10}Be data suggest drying in the Atacama after ~ 4.7 Ma, and returning to an insignificant wet period at ~ 1 Ma, which was possibly connected to El Niño- or La Niña-like climate change.
© 2015 Published by Elsevier Ltd.

1. INTRODUCTION

The mechanism of soil formation in hyper-arid regions and its connection to climate have only recently been investigated (*e.g.* Ewing et al., 2006) but remain poorly understood. Soil formation is commonly driven by several key processes, *i.e.* incorporation of organic matter, break-down of bedrock, atmospheric deposition, weathering, erosion and transportation of solutes (Chadwick et al., 1990). In hyper-arid regions, such as the driest parts of the Atacama Desert, Chile (mean annual precipitation < 2 mm) (Hartley and Chong, 2002; Rech et al., 2006), biological activity and water-related processes are limited, and soil

formation may enter into a new paradigm: simple long term accumulation of atmospheric deposition ("dust"), *i.e.* eolian sediment, airborne particles and photochemical products (Ewing et al., 2006; Wang, 2013). Similar soil formation processes have also been postulated for the Martian surface (Amundson et al., 2008). This mechanism is supported by recent isotopic studies showing that deposits of oxy-anions (e.g. NO_3^- and SO_4^{2-}) in the Atacama soils are primarily derived from photochemically produced secondary aerosols (Böhlke et al., 1997; Bao et al., 2004; Michalski et al., 2004; Ewing et al., 2007, 2008b). However, details about the factors such as the timescale of soil accumulation and influence of past climate in hyper-arid regions remain uncertain.

Establishing the timescale of soil formation in the Atacama has proved challenging. Previous efforts have focused on surface exposure dating (Ewing et al., 2006) or

---

* Corresponding author. Fax: +1 765 496 1210.
E-mail address: gmichals@purdue.edu (G. Michalski).

dating of volcanic ash layers (Rech et al., 2006; Placzek et al., 2009), but both approaches are subject to uncertainties and limitations. Inferring a soil's age using cosmogenic nuclides produced in exposed clasts or boulders is based on the assumption that they originate from the parent rock and have coevolved with the soil, giving the age of the whole soil profile (Anderson et al., 2002). The total soil depth, however, is not always known, and potential prior exposure or disturbance of surface boulders/clasts can result in additional or reduced cosmogenic nuclide accumulation (Gosse and Phillips, 2001), both leading to poorly constrained ages. Volcanic ash layers are rare, often spatially discontinuous, and only provide the maximum ages of their overlying soil profile (Placzek et al., 2009). Therefore, new techniques are warranted for constraining the soil formation timescales in the Atacama.

Hyper-aridity has likely prevailed in the Atacama for millions of years (Hartley and Chong, 2002; Rech et al., 2006), but sporadic changes in rainfall rates are believed to have occurred over time (Betancourt et al., 2000; Gayo et al., 2012) and could have had a significant influence on soil formation. In hyper-arid regions, any short term increase in rainfall can increase atmospheric inputs via wet deposition accordingly. Similarly, soil erosion by water can also be accelerated by torrential storms and outwash (Haug et al., 2010; Amundson et al., 2012), while part of the rainfall can percolate through the soil profile to promote the losses of dissolved materials by way of deep seepage (Jenny, 1941). Ewing et al. (2006) demonstrated that increasing rainfall may induce a shift in the soil formation mechanism from a continuous accumulation of atmospheric solutes with a dramatic volumetric expansion to a net mass loss and volumetric collapse. Owen et al. (2011) and Jungers et al. (2013) indicated that climatic effects could have been an important control of surface erosion and deposition processes and the source material of sediment. In addition, pulses of water in the Atacama may induce viable soil microorganisms to become biologically active and initiate carbon and nitrogen fixation (Warren-Rhodes et al., 2006; Ewing et al., 2008a; Azua-Bustos et al., 2012). Amit et al. (2010) also suggested that the depletion of soluble salts in the soil profile caused by precipitation-induced leaching may prevent soil salinization and enable vegetation establishment in hyper-arid regions. However, highly resolved temporal shifts in the Atacama's climate have been difficult to assess.

Precipitation in the Atacama is sensitive to climatic shifts caused by a variety of factors. The aridity in the Atacama is caused by two mountain barriers, the Coastal Range to the west and the Andes to the east, which create rain shadow effects, blocking moisture from the Pacific and Amazonia, respectively. In addition, the quasi-permanent southeast Pacific subtropical anticyclone and the cold Peru Current generate low sea surface temperatures causing a temperature inversion and thus limited rainfall (Houston and Hartley, 2003). However, Atacama aridity can be altered by heavy rainfall episodes related to El Niño–Southern Oscillation (ENSO) characterized by a weakened subsiding branch of the Pacific Walker circulation and strong positive sea surface temperature anomalies

(Vargas et al., 2000; Garreaud et al., 2003; Houston, 2006). Historical records suggested that there were persistent ENSO instabilities throughout the entire last glacial–interglacial cycle, but assessing the ENSO modulation dynamics has been largely speculative and limited to model predictions or rare terrestrial climate proxies (Clement et al., 2001). These proxies, however, gave different and sometimes conflicting results about precipitation variability in arid regions over time (Joubert and Hewitson, 1997; Hulme et al., 2001; Covey et al., 2003; Hewitson and Crane, 2006). Therefore, new precipitation proxies from the Atacama Desert would be useful for detecting regional precipitation variations and their teleconnections to global climate oscillations.

Meteoric beryllium-10 (^{10}Be) has been used in other environments to, with some uncertainties, constrain soil ages and detect climate change (cf. Willenbring and von Blanckenburg, 2010). Meteoric ^{10}Be is produced by spallation of nitrogen and oxygen atoms by secondary cosmic rays in the stratosphere and becomes quickly attached to aerosols (Lal, 1987). When these aerosols are delivered to soil surfaces by dry or wet deposition, ^{10}Be usually becomes bound to soil clay minerals and iron oxy-hydroxides. The deposited ^{10}Be then decays with a radioactive half-life of 1.39 My (Chmeleff et al., 2010). Thus, concentrations of meteoric ^{10}Be in soils reflect a balance between inputs, outputs, and decay over time.

Soil ages have been calculated based on the meteoric ^{10}Be inventory and deposition rate (Graly et al., 2010; Willenbring and von Blanckenburg, 2010), but there are several challenges using the inventory approach. This approach assumes that all of the meteoric ^{10}Be deposited during the history of the soils is retained and only subject to decay loss. Potential ^{10}Be losses by erosion or leaching as well as incomplete sampling of the entire soil profile, suggests a soil age can only be considered as a minimum age because of the underestimation of the meteoric ^{10}Be inventory (e.g. Pavich and Vidic, 1993). Also, the meteoric ^{10}Be production changes over time because of shifts in solar activity, weakening/strengthening of the interplanetary magnetic field and geomagnetic field intensity, thus altering the ^{10}Be deposition rate (e.g. Masarik and Beer, 2009). Shifting ^{10}Be delivery rates that accompany climate change (e.g. Lal, 1987) can also complicate estimating the meteoric ^{10}Be deposition rate and result in uncertainties in soil age calculation. This climate effect, however, may be a way to use ^{10}Be as a proxy to explore the climate change over time, though caution is warranted (e.g. Gu et al., 1996; Graham et al., 2001).

Some of the processes that normally control meteoric ^{10}Be flux are not significant in the Atacama, which present a unique challenge and opportunity for the application of meteoric ^{10}Be. In most soils, meteoric ^{10}Be is mainly deposited as a solute in rain and it typically migrates down the soil profile (Brown et al., 1992). This redistribution to depth helps minimize ^{10}Be loss at the surface during wind erosion. However, this mechanism is probably not at play in the Atacama where dry deposition is much greater than wet deposition and downward leaching is minimized by the hyper-aridity. We hypothesize that in some regions of the

Atacama, soil accretes mainly via atmospheric deposition over time, and as such also builds up meteoric [10]Be. Since [10]Be solubility is negligible in alkaline soils, there will be negligible downward movement, and thus it may be a tracer of the timescale of soil formation in the Atacama based on its decay property, while there may be some climate-induced deviations from the [10]Be decay trend. Therefore, we have utilized meteoric [10]Be concentrations with depth to assess the mechanism and timescale of Atacama soil development and to detect any evidence of climatic change.

2. SITE AND SOIL DESCRIPTIONS

The sampled soil profile was from a temporary 225 cm deep pipeline trench (22.88°S, 69.64°W, 1500 m a.s.l) located in the central longitudinal depression of the Atacama that is called the "Central Valley". The Central Valley is a result of the uplift of the coastal Range to the west and the Andes mountains to the east over the past 30 million years (Moreno and Gibbons, 2007). The trench surface is covered with sparse desert pavements of moderately varnished gravel to cobble-sized clasts and ventifacts and there is no evidence of vegetation or water erosion. The surface has been previously interpreted as an alluvial fan of upper Miocene–Pliocene piedmont sediments (SERNAGEOMIN, 2003) that mantles rocks of Jurassic and Cretaceous age (Ericksen, 1983) (Fig. 1). The 24-year mean annual precipitation (50 km to the north) was 0.4 mm (Houston, 2006).

The trench soil profile consists of two horizons: an upper layer (0–15 cm) comprised of blocks of moderately-cemented gypsum and sand with vertical cracks at spatial intervals of 10–30 cm, and a lower layer that was vesicular and dusky yellow (Munsell color system: 5Y 6/4)

containing loosely-cemented sands and fragile aggregates (Figs. 1 and 2). This was a relatively simple structure compared to the soil profile in the nearby Yungay region (24.10°S, 70.02°W, 153 km southwest, Fig. 1) described by Ewing et al. (2006).

3. METHOD

Forty-three samples were collected at ~5 cm vertical resolution in the lower layer of the soil profile, while the surface gypsum block layer was disturbed during excavation and thus not sampled. The soil density was calculated by slightly compacting 10 g soil into a graduated measuring cylinder. The salt-cemented soil aggregates were gently broken up and a dry sieve analysis was conducted to study the grain size distribution with depth. One gram of bulk soil (<2 mm fraction) was weighed, powdered by a ball mill, and soluble salts were extracted with 45 mL Millipore water using vortex mixing. Cation (Ca^{2+}, Na^+, K^+ and Mg^{2+}) concentrations in the soil extracts were determined using Thermo Scientific iCAP 6500 inductively coupled plasma-optical emission spectroscopy (ICP-OES). Dionex DX-500 ion chromatography with suppressed conductivity detector (Alltech 626 model) was used for anion analysis (Cl^-, NO_3^- and SO_4^{2-}). The measurement uncertainties for different ion concentrations in this study were typically <5% based on replicate analysis of standards and calibrations.

Atmospheric deposition was collected using two passive dust traps installed at two adjacent sites (<30 km distance), which were chosen on the basis of absence of dirt roads and inconspicuousness. The traps consist of a single-piece Bundt cake pan fitted with a circular piece of 1/4-inch-mesh galvanized screen on which a dense layer of pre-washed glass marbles suspend to mimic desert pavements on the
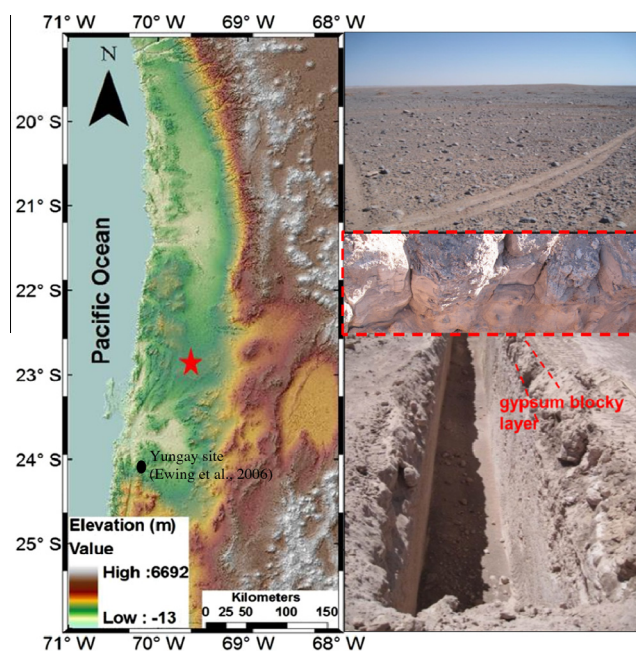

Fig. 1. Site location (red star) and field pictures of the surface and the profile (the right middle picture and between dash lines: gypsum block layer). (For interpretation of the references to color in this figure legend, the reader is referred to the web version of this article.)
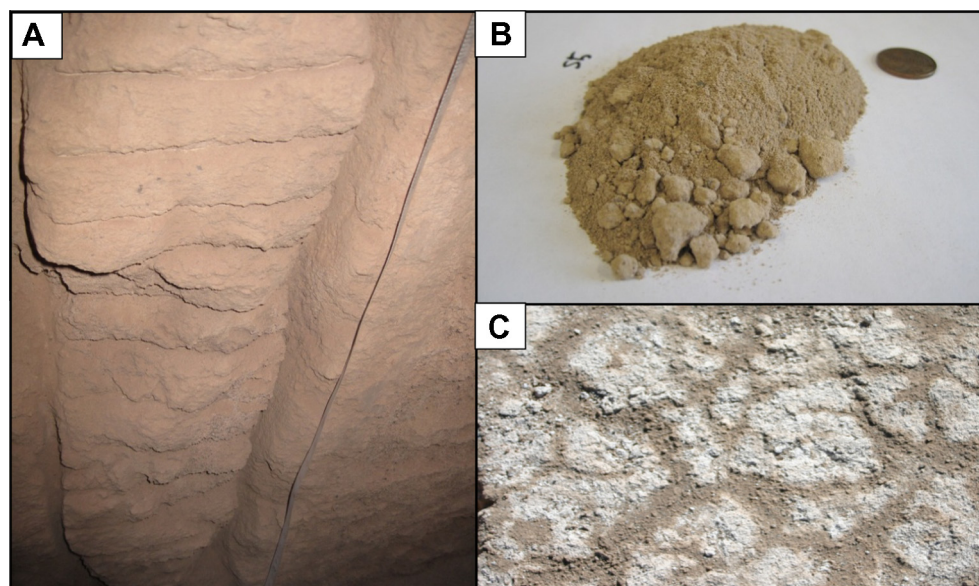
Fig. 2. Soil pictures (A) The loosely-cemented sand unit liable to hand sampling; (B) The close-up picture for the sample at 35 cm (Note: the color of the sample in the picture may slightly differ from the actual sample); (C) The vertical view for the surface gypsum layer typical in the surrounding regions. (For interpretation of the references to color in this figure legend, the reader is referred to the web version of this article.)

surface (Reheis and Kihl, 1995). The traps were mounted on ~1 m high poles above the ground to eliminate most saltating particles. Atmospheric deposition during the rainless period 7/10/2007-1/1/2010 (DGA, 2011) was recovered by rinsing the pan and marbles with Millipore water. The rinse solution was kept at 0 °C and then shipped frozen overnight to Purdue University. The frozen solution was freeze-dried, and the resulting solids were weighed. The solid material was re-suspended in Millipore water and filtered to remove water soluble ions, and the insoluble fraction was dried and weighed again. The trap extract was also analyzed using ICP-OES and ion chromatography for cation and anion concentrations, and preliminary data indicated that water-soluble salts comprise $39 \pm 7\%$ of the dust mass (Wang et al., 2014).

The bulk soils and dust residues (water-soluble salts being removed) were inspected for particle shape and appearance under microscopy, determined of the mineralogy on the basis of the powder X-ray diffraction patterns, and then analyzed for ^{10}Be concentrations. They were sieved and 0.5–1 g of the <2 mm fraction was leached using 10–20 ml 0.5 M HCl at 60 °C for six hours. The leachate should contain only meteoric ^{10}Be because the samples were not subjected to physical treatment or HF decomposition, and the acid was too weak to liberate $in\ situ$-produced ^{10}Be that is typically incorporated inside the quartz minerals. After ^{9}Be carrier addition, the Be was separated by EDTA titration, cation exchange, and pH-specific precipitation following a conventional technique ($e.g.$ Granger et al., 2001). ^{10}Be/^{9}Be ratios were determined by accelerator mass spectrometry (AMS) at the Purdue Rare Isotope Measurement (PRIME) laboratory based on the revised ICN ^{10}Be standard (Nishiizumi et al., 2007). The AMS measurement uncertainties were controlled to be ⩽7%. The average ^{10}Be amount in blank controls of $3.88 \pm 1.37 \times 10^5$ atoms ($n = 7$) was subtracted from all

samples. All reported ^{10}Be concentrations were normalized to insoluble fractions in soils or atmospheric dust (see Table 1 for detailed analytical data).

4. RESULTS

An average soil density was 1.4 g cm^{-3}. The major mineral assemblages for the bulk soil and dust residue are quartz-anorthite-albite, with intermittent existence of halite, nitratine or gypsum at several depths for the soils. The soil and dust particles were all angular and not frosted. The dry soil was composed of $4 \pm 4\%$ gravels (>2 mm), $91 \pm 10\%$ sands (63 μm–2 mm) and $5 \pm 2\%$ silt and clay (<63 μm) by mass (Fig. 3). The soil was rich in Cl$^-$, NO$_3^-$ and SO$_4^{2-}$ anions, and their concentration peaks were observed at depths of ~200 cm (Fig. 3). The mass content of water-insoluble fractions, obtained by subtracting the cation and anion (including completely extracted gypsum) contents measured by ICP-OES and ion chromatography, was ~90% for each soil sample. The ^{10}Be concentration in atmospheric dust was $1.24 \pm 0.19 \times 10^8$ atoms g^{-1}, and the bulk and insoluble dust deposition rates based on dust trap analysis were $7.8 \pm 1.8 \times 10^{-4}$ g cm^{-2} yr^{-1} and $3.0 \pm 0.2 \times 10^{-4}$ g cm^{-2} yr^{-1} ($n = 2$), respectively. The measured soil ^{10}Be concentrations exponentially decreased with depth (Fig. 4). The highest values ($1.36–1.45 \times 10^8$ atoms g^{-1}) occurred near the surface, and the lowest concentrations ($4.78–6.90 \times 10^6$ atoms g^{-1}) were at the bottom of the profile. There were small but significant deviations from the exponential decrease at depths of approximately 25, 75, 100 and 175 cm.

5. DISCUSSION

There are at least two possible mechanisms that can explain the observed exponential decrease in soil ^{10}Be

Table 1
Analytical results of meteoric ^{10}Be profile.

Sample[a,b]	Depth (cm)	Soil mass (g)	Be carrier (mg)	^{10}Be/Be[c,d] ($\times 10^{-15}$)	^{10}Be concentrations [e,f] (10^7 atoms g^{-1} bulk soil)	Insoluble fraction[g] (%)	^{10}Be concentrations[h] (10^7 atoms g^{-1} insoluble frac.)
Atmospheric deposition	0	0.5009	0.3770	2224.16 ± 338.54		62.33	12.36 ± 1.90
LT1	15	0.5057	0.3762	2252.62 ± 64.84	12.38 ± 0.36	91.20 ± 4.56	13.57 ± 0.84
LT2	20	0.5074	0.3755	2340.00 ± 80.00	12.89 ± 0.44	92.21 ± 4.61	13.98 ± 0.90
LT3	25	0.5064	0.3760	2443.43 ± 139.80	13.35 ± 0.77	92.29 ± 4.61	14.47 ± 1.14
LT4	30	0.5054	0.3766	2312.66 ± 69.30	12.75 ± 0.39	92.39 ± 4.62	13.80 ± 0.86
LT5	35	0.5043	0.3777	2285.24 ± 60.43	12.65 ± 0.34	92.86 ± 4.64	13.63 ± 0.82
LT6	40	0.5033	0.3773	1982.34 ± 56.39	10.97 ± 0.32	90.74 ± 4.54	12.09 ± 0.75
LT7	45	0.5047	0.3773	1476.02 ± 50.52	8.15 ± 0.28	90.30 ± 4.52	9.02 ± 0.59
LT8	50	0.5024	0.3807	1150.00 ± 40.00	6.41 ± 0.23	89.30 ± 4.47	7.18 ± 0.48
LT9	55	0.5053	0.3779	1300.00 ± 50.00	7.10 ± 0.28	89.50 ± 4.48	7.93 ± 0.54
LT10	60	0.5046	0.3786	1330.00 ± 80.00	7.34 ± 0.45	90.46 ± 4.52	8.11 ± 0.67
LT11	65	0.5020	0.3692	1058.20 ± 53.05	5.69 ± 0.29	93.29 ± 4.66	6.09 ± 0.45
LT12	70	1.0053	0.4974	1286.98 ± 74.45	4.73 ± 0.28	93.04 ± 4.65	5.08 ± 0.40
LT13	75	1.0072	0.5121	885.53 ± 52.81	3.37 ± 0.20	94.89 ± 4.74	3.55 ± 0.29
LT14	80	1.0074	0.5078	773.00 ± 18.84	2.91 ± 0.07	95.90 ± 4.80	3.03 ± 0.18
LT15	85	1.0054	0.5208	699.70 ± 18.90	2.80 ± 0.08	95.43 ± 4.77	2.94 ± 0.17
LT16	90	1.0066	0.5152	901.99 ± 27.98	3.53 ± 0.11	94.23 ± 4.71	3.74 ± 0.23
LT17	95	1.0057	0.5145	855.45 ± 25.98	3.26 ± 0.10	94.56 ± 4.73	3.45 ± 0.21
LT18	100	0.5086	0.3747	840.75 ± 48.88	4.51 ± 0.27	94.34 ± 4.72	4.78 ± 0.38
LT19	105	0.5049	0.3733	420.48 ± 18.55	2.23 ± 0.11	94.76 ± 4.75	2.35 ± 0.17
LT20	110	0.5033	0.3736	219.91 ± 15.57	1.07 ± 0.09	95.02 ± 4.75	1.13 ± 0.11
LT21	115	0.5087	0.3744	292.32 ± 13.02	1.51 ± 0.08	96.11 ± 4.81	1.57 ± 0.11
LT22	120	1.0339	0.5129	325.33 ± 11.81	1.15 ± 0.05	94.16 ± 4.71	1.23 ± 0.08
LT23	125	0.5094	0.3751	473.36 ± 33.41	2.50 ± 0.19	95.34 ± 4.77	2.63 ± 0.24
LT24	130	0.5030	0.3769	444.35 ± 14.33	2.27 ± 0.08	96.04 ± 4.80	2.37 ± 0.15
LT25	135	0.5053	0.3763	330.64 ± 15.80	1.75 ± 0.09	95.89 ± 4.79	1.82 ± 0.14
LT26	140	0.5055	0.3762	320.28 ± 14.85	1.68 ± 0.09	96.30 ± 4.81	1.75 ± 0.13
LT27	145	0.5046	0.3774	332.23 ± 19.87	1.76 ± 0.11	95.08 ± 4.75	1.85 ± 0.15
LT28	150	0.5034	0.3774	196.98 ± 14.66	1.01 ± 0.09	95.41 ± 4.77	1.06 ± 0.11
LT29	155	0.5020	0.3759	270.49 ± 12.34	1.42 ± 0.07	92.22 ± 4.61	1.54 ± 0.12
LT30	160	0.5075	0.3799	249.37 ± 15.35	1.30 ± 0.09	93.25 ± 4.66	1.39 ± 0.12
LT31	165	0.5049	0.3759	423.17 ± 16.11	2.26 ± 0.09	92.86 ± 4.64	2.44 ± 0.17
LT33	175	1.0252	0.5130	490.09 ± 15.45	1.78 ± 0.06	94.39 ± 4.72	1.88 ± 0.12
LT34	180	1.0282	0.5212	542.22 ± 17.50	2.00 ± 0.07	89.74 ± 4.49	2.23 ± 0.15
LT35	185	0.5040	0.3722	391.92 ± 10.78	2.07 ± 0.07	92.98 ± 4.65	2.22 ± 0.14
LT36	190	1.0255	0.5130	407.38 ± 11.63	1.48 ± 0.05	92.06 ± 4.60	1.61 ± 0.10
LT37	195	1.0268	0.5130	157.66 ± 9.36	0.54 ± 0.04	91.47 ± 4.57	0.59 ± 0.05
LT38	200	1.0245	0.5139	171.32 ± 8.36	0.59 ± 0.03	85.55 ± 4.28	0.69 ± 0.06
LT39	205	1.0252	0.5144	194.96 ± 7.58	0.68 ± 0.03	89.45 ± 4.47	0.77 ± 0.06
LT40	210	0.5046	0.3721	167.73 ± 14.64	0.84 ± 0.08	82.98 ± 4.15	1.01 ± 0.12
LT41	215	0.5053	0.3730	85.22 ± 6.15	0.38 ± 0.05	67.83 ± 3.39	0.56 ± 0.08
LT42	220	0.5043	0.3728	119.15 ± 5.86	0.57 ± 0.04	82.16 ± 4.11	0.69 ± 0.07
LT43	225	0.5068	0.3758	97.47 ± 4.78	0.45 ± 0.04	94.67 ± 4.73	0.48 ± 0.05

[a] Samples LT1–43 were from a trench (22.88°S, 69.64°W, elevation: 1500 m). The sample of LT32 was missing during the transport.

[b] Atmospheric deposition sample was the combined sample collected by two dust collectors from two adjacent sites (22.84°S, 69.70°W, 1486 m and 23.01°S, 69.39°W, 1480 m).

[c] Isotope ratios were normalized to the ICN standard Be-01-5-2 with a ratio of 8.558×10^{-12}.

[d] Uncertainties are reported at the 1σ confidence level.

[e] A mean blank value of 388,184 ± 137,435 ^{10}Be atoms (^{10}Be/^{9}Be = 14.29 ($\pm$5.91) $\times 10^{-15}$) was used to correct for carrier background.

[f] Propagated uncertainties from uncertainties in blank and AMS analytical errors.

[g] The insoluble soil fractions were obtained by subtracting cation and anion contents measured by inductively coupled plasma optical emission spectroscopy (ICP-OES) and ion chromatography with propagated uncertainty of 5%, while the insoluble fraction in atmospheric dust was the mass difference between before and after removing soluble salts.

[h] Propagated uncertainties from uncertainties in blank, insoluble fraction and AMS analytical error.
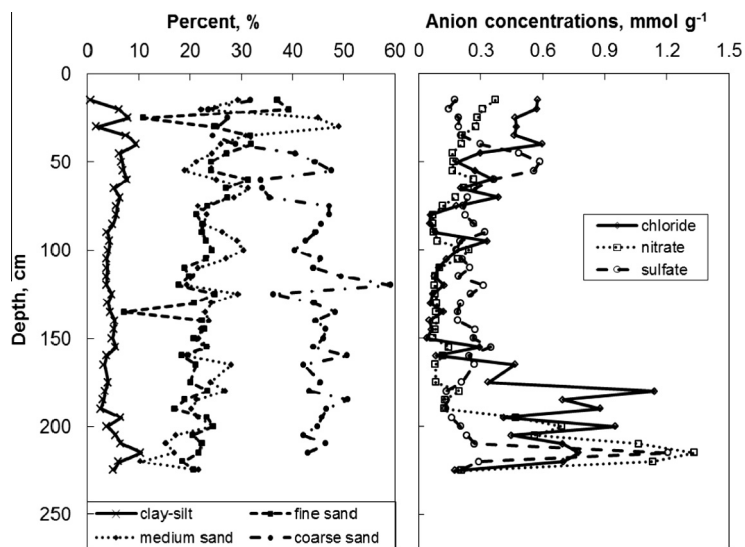
Fig. 3. The comparison of grain size distribution and anion depth profiles.
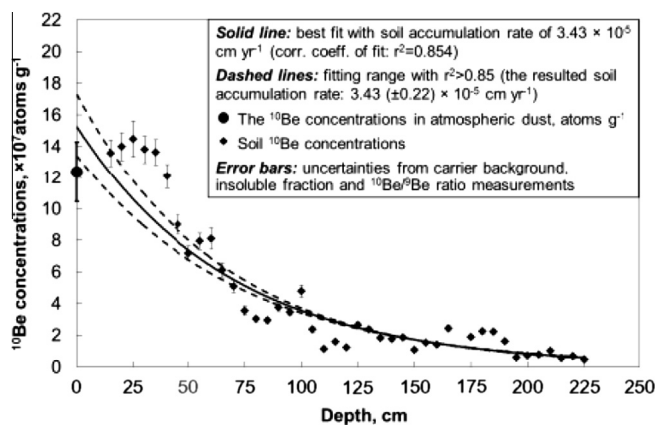

Fig. 4. The Atacama soil [^{10}Be] depth profile and the exponential fittings of the data according to Eq. (4).

concentrations with soil depth and each gives a different estimate of the soil age. The first is the surface accumulation of meteoric ^{10}Be on an existing parent alluvium followed by the downward migration of ^{10}Be via solute or physical transport. The timescale for soil accumulation based on this mechanism can be evaluated using the ^{10}Be inventory method. The second mechanism is that the soil has developed via the net retention of atmospheric dust and sand containing meteoric ^{10}Be and the ^{10}Be radioactively decays *in situ* over time. In this case, the timescale of soil development is estimated by assuming ^{10}Be is deposited in layers and complies with the law of radioactive decay. In the following discussion, we evaluate both mechanisms and suggest the latter mechanism is more probable.

5.1. The existing parent alluvium mechanism

The existing parent alluvium mechanism assumes that meteoric ^{10}Be is deposited on the surface of an existing parent alluvium and transported down profile. It could be suggested that the observed exponential decrease in soil ^{10}Be

concentrations be explained by downward transport of ^{10}Be via a diffusion process. However, diffusion would require a water saturated profile for at least the timescale of diffusion over the 225 cm depth (~160 years, L^2/D; $L = 225$ cm, $D_{ion} = 1 \times 10^{-9}$ m s^{-2}) (Samson et al., 2003). This seems unlikely given multiple studies that suggest hyper-aridity, with precipitation less than 2 mm/yr, on million-year timescales (Hartley and Chong, 2002; Rech et al., 2006). In addition, if one compound is being controlled by diffusion, then all soluble species must also be diffusion limited. Sufficient water to weather or mobilize ^{10}Be would solubilize soluble minerals, such as halite (NaCl), and purge them from the upper sections of the profile. However, the presence of significant amounts of highly soluble Cl$^-$ and NO$_3^-$ and even marginally soluble SO$_4^{2-}$ in the upper sections refute a diffusive mechanism (Fig. 3). Third, the model would also require all the ^{10}Be to be deposited at one time, which is unlikely (see Section 5 about the ^{10}Be inventory method-based age estimate). Finally, a diffusion model requires the soil matrix to be established prior to the deposition. Tuffs in the regions dated to 2–6.6 Ma have 2–4 m of

overburden (Placzek et al., 2009), which would have taken significant time to accumulate. This accumulation time is also evident in salt accumulation (Michalski et al., 2004; Wang, 2013). This suggests that there was no established soil matrix for the diffusion to occur. Therefore, a diffusion model could not account for the observed ^{10}Be concentration profile.

Alternatively, the ^{10}Be downward migration could occur during periods of enhanced precipitation, and the soil ^{10}Be concentration distribution could be related to the probability of precipitation. This is supported by observed changes in the [Cl$^-$] with depth, which shows several discrete bulges (Fig. 3) and may correspond to excess ^{10}Be relative to the exponential line. In this scenario, soluble salts along with micron-sized silicate and ^{10}Be particles accumulate near the surface during periods of high aridity. A shift to a wetter climate is capable of leaching highly soluble salts down profile carrying with them a small fraction of ^{10}Be while leaving behind less soluble gypsums and the majority of the ^{10}Be. Lower ^{10}Be activities at depths would then be due to a lower probability of high precipitation rates needed to mobilize the particles and *in situ* decay if the precipitation occurred in the past. However, soil age, mass balance, and solubility considerations argue against such a mechanism (see below for detailed Section 5).

In order to evaluate whether the estimated soil age using the ^{10}Be inventory and the parent alluvium mechanism was comparable to other regional surface ages (Ewing et al., 2006; Rech et al., 2006; Placzek et al., 2009, 2010), the ^{10}Be flux was evaluated. The meteoric ^{10}Be flux to the surface was estimated using the dust trap data. The modern meteoric ^{10}Be flux (F$_{10Be}$) was derived as:

$$F_{10Be}(\text{atoms cm}^{-2}\text{yr}^{-1}) = [^{10}\text{Be}]_{\text{dust}} \times D_{dust} \qquad (1)$$

where $[^{10}\text{Be}]_{\text{dust}}$ is the observed $1.24 \pm 0.19 \times 10^8$ atoms•(g insoluble dust)$^{-1}$ and D_{dust} is the observed insoluble dust deposition rate of $3.0 \pm 0.2 \times 10^{-4}$ g (insoluble dust) •cm^{-2} •yr^{-1}. This yields a F$_{10Be}$ of $3.7 \pm 0.6 \times 10^4$ atoms cm^{-2} yr^{-1} (see the uncertainty discussion of this value below about the dust flux). This flux is only 6% of the current estimated global average ^{10}Be deposition rate of $\sim 5.8 \times 10^5$ atoms cm^{-2} yr^{-1} (Masarik and Beer, 2009; Field et al., 2006; Heikkilä, 2007) and about one order of magnitude lower than the ^{10}Be deposition estimates for the Atacama region with the long term solar modulation and geomagnetic field (Field et al., 2006; Heikkilä, 2007; Willenbring and von Blanckenburg, 2010). These global models, however, clearly overestimated ^{10}Be in the Atacama because the coarse horizontal resolution (>300 km) poorly represents the Atacama's narrow (~80 km) hyper-arid region. This bias assigns a high ^{10}Be flux by wet deposition to a region that is essentially rainless. For example, the ECHAM5-HAM model predicted that the precipitation at the sampling site is greater than 2 mm per day (Heikkilä and Smith, 2013), when in fact the long term average precipitation at our site is less than 2 mm per year (Hartley and Chong, 2002; Rech et al., 2006). The same model predicted a modern ^{10}Be dry deposition rate ~6 × 10^4 atoms cm^{-2} yr^{-1} in the Atacama (Heikkilä and Smith, 2013), in near agreement with our measured flux

of $3.7 \pm 0.6 \times 10^4$ atoms cm^{-2} yr^{-1}. The F$_{10Be}$ at our field site is also comparable to the low ^{10}Be flux of $\sim 1 \times 10^4$ atoms cm^{-2} yr^{-1} observed in the Dry Valley of Antarctica, which has a similar hyper-arid climate (Bettoli et al., 1993). Thus, the significantly lower ^{10}Be deposition rate at the field site relative to the global average is because the usual scavenging of ^{10}Be from the atmosphere by wet deposition is essentially absent in the Atacama's hyper-arid environment.

The F$_{10Be}$ can then be used to estimate the soil age via the soil ^{10}Be inventory. The inventory of meteoric ^{10}Be in our 225 cm deep profile (I) was estimated by:

$$I = \Sigma \rho \bullet l \bullet [^{10}\text{Be}] \qquad (2)$$

where ρ is the soil density of 1.4 g cm^{-3} and l is the sample length of 5 cm. This leads to $\sim 1.3 \times 10^{10}$ atoms cm^{-2} (1.2×10^{10} atoms cm^{-2} with the surface 10 cm samples and another sample at 170 cm missing, Table 1). If there is no erosion or leaching losses of ^{10}Be in the soil profile, the soil ^{10}Be inventory should only relate to the meteoric ^{10}Be flux F$_{10Be}$ and soil age (t) (Willenbring and von Blanckenburg, 2010) as: $I = F_{10Be}/\lambda \bullet [1-\exp(-\lambda t)]$. By assuming a constant F$_{10Be}$ of 3.7×10^4 atoms cm^{-2} yr^{-1} as calculated above, the soil age can then be estimated as (Graly et al., 2010):

$$t = (-1/\lambda) \bullet \ln(1 - \lambda I/F_{10Be}) \qquad (3)$$

The resulting soil age would be 386 ky.

The ^{10}Be inventory derived soil age is generally not in line with the age of soils found in nearby locations in the Atacama. For example, roughly 70 km southwest of our site, a tuff layer overlain by ~4 m thick coarse alluvial sediment has an estimated age of 6.67 ± 0.13 Ma (Placzek et al., 2009). Rech et al. (2006) reported *ca.* 19–13 Ma salic gypsisols at the depths of 2–31 m located ~90 km east of our site. Many stable landforms in central Atacama have surface exposure ages (1.5–2.6 Ma) (Ewing et al., 2006; Placzek et al., 2010). It seems unlikely that the age of the soil at the study site is a factor of 10 younger than those on similar nearby landscapes. Instead, it may be due to the uncertainties associated with the age estimate using the soil ^{10}Be inventory related to the approach's inherent assumptions that meteoric ^{10}Be deposition rate is constant and all of the meteoric ^{10}Be deposited is retained and only subject to decay loss as detailed in Section 1 (Graly et al., 2010).

Scaling the dust trap deposition rate of $7.8 \pm 1.8 \times 10^{-4}$ g cm^{-2} yr^{-1} and the 386 ky age based on a ^{10}Be accumulation mechanism suggests that ~300 g cm^{-2} material has been deposited. Applying the site's average soil bulk density of 1.4 g cm^{-3} gives an accumulation of 2.1 m, approximately the depth of the soil trench. Thus for the existing parent alluvium mechanism to be applicable, all of the ^{10}Be would have been retained while all of the dust deposition must have been eroded away by wind. This seems unlikely, especially when considering that ^{10}Be is usually strongly held by the solid particles and ^{10}Be solubility may limit the free movement of ^{10}Be under certain conditions. The distribution coefficient K_d of ^{10}Be (the ratio of ^{10}Be amounts in particulate and dissolved phases) is

10^5–10^6 (Balistrieri and Murray, 1986; You et al., 1989) and can be as high as 10^7 (Li et al., 1984) at neutral pH. The binding of ^{10}Be to soil particles, however, is strongly pH dependent and decreases rapidly by four orders of magnitude between pH 6 and 2 (You et al., 1989). The Atacama soils were neutral to alkaline (pH = 7~9) (preliminary data) and at these pHs, most Be was likely present as Be(OH)$_2$ or its hydrolyzed species (Willenbring and von Blanckenburg, 2010) that are essentially water-insoluble ($K_{sp} = 6.92 \times 10^{-22}$ mol^3 L^{-3} at 25 °C for Be(OH)$_2$) (Haynes, 2014). If gypsum ($K_{sp} = 3.14 \times 10^{-5}$ mol^2 L^{-2}) (Haynes, 2014), which compared to Be is highly soluble, is retained at the surface, a mechanism that mobilizes Be but not gypsum is difficult to envision.

Physical transport of ^{10}Be attached to small grains rather than dissolution in a pre-existing sandy alluvium also cannot be the major mechanism. As the mineralogy and morphology of the dust and soil particles are similar, it is difficult to assume they have different origins. Also, as discussed above, with the simultaneous deposition of ^{10}Be and sand-like dust particles, the retention of ^{10}Be-attached fine particles but losses of dust particles could not be explained and would bring questions regarding the destination of the dust particles. Furthermore, if a sandy parent alluvium existed before the deposition of ^{10}Be-attached fine particles, we should expect to see a textural change rather than a relatively consistent grain size distribution. A profile with ^{10}Be concentration bulges associated with random dust particle movement would be more probable than an exponential decay trend of ^{10}Be concentrations with depth (Figs. 3 and 4). Therefore, the hypothesis of an existing parent alluvium and ^{10}Be downward transport can be largely refuted, and the observed exponential decrease in soil ^{10}Be concentrations with depth cannot be explained by the mechanism of an existing parent alluvium and the subsequent downward movement of ^{10}Be.

5.2. The layer-like accumulation mechanism

An alternative model for interpreting the decrease of meteoric ^{10}Be concentrations with depth is that soil matrix containing meteoric ^{10}Be accumulates in layers via the deposition of atmospheric dust and the ^{10}Be radioactively decays in situ over time. This hypothesized soil accumulation mechanism is consistent with the pedogenic process in the Mojave Desert proposed by McFadden et al. (1987) and Anderson et al. (2002). It suggests that atmospheric salts are an important agent of rock weathering, breaking down the bedrock material in the presence of only trace amounts of moisture (Cooke, 1981; Goudie et al., 2002). This enables atmospheric dust to infill between bedrock fractures that further enhances the bedrock weathering and material gains. This separation of the surface fragments from the bedrock initiates the development of a desert pavement (McFadden et al., 1987) that begins to trap atmospheric dust underneath, leading to the development of a cumulate soil over time. Over time, the clasts become completely isolated from the bedrock as the accrued soil continuously elevates them, resulting in a classic desert pavement.

In the Atacama, low solubility gypsum/anhydrite crusts slowly evolve into a columnar, blocky layer (Fig. 1) that stabilizes soils in a way that is similar to desert pavements. The Ca^{2+} and SO$_4^{2-}$ found in Atacama soils are likely derived from ocean aerosols that deposit to the surface and then precipitate as gypsum during rare and small rainfall events (Rech et al., 2006; Ewing et al., 2008b; Wang et al., 2014). Similar to desert pavements, these gypsum crusts can trap and stabilize atmospheric dust, including ^{10}Be adhered to silicate dust. Thermal fracturing of these gypsum crusts would allow bound ^{10}Be to migrate down through the cracks (Fig. 2C), which would then isolate it from potential wind erosion. This would enable the dust and ^{10}Be to accumulate and result in the inflation of the soil profile over time nearly as discrete layers (Fig. 5). This inflation of Atacama soils by atmospheric deposition of salts and silicate minerals was previously suggested by Ewing et al. (2006) but they were unable to discern the rate of silicate mineral accumulation. This accumulation mechanism can then explain the decreasing meteoric ^{10}Be concentrations with depth as a deposition followed by in situ ^{10}Be decay. This mechanism is unlike most soil ^{10}Be accumulation models where atmospheric deposition infiltrates a pre-existing parent alluvium and is more analogous to a micro-scale loess deposit that accrues mass (soluble and insoluble) over time.

In this simple layer-like accumulation model, assuming a relatively constant long term soil accumulation rate a (cm yr^{-1}), the age of each soil layer t (yr) can be established as a function of depth h (cm) using $t = h/a$. Considering ^{10}Be decays exponentially with time according to the law of radioactive decay (Arthur et al., 1981), there would be an exponential decrease in soil ^{10}Be concentration ([^{10}Be]) with depth:

$$[^{10}\text{Be}] = [^{10}\text{Be}]_i \exp(-\lambda h/a) \qquad (4)$$

where [^{10}Be]$_i$ is ^{10}Be concentration in the surficial soil without decay (i.e. ^{10}Be concentration in atmospheric dust), and λ is the ^{10}Be decay constant (4.9975×10^{-7} yr^{-1}).

This simple accumulation-decay model reproduces the ^{10}Be data remarkably well. When the data are fitted with
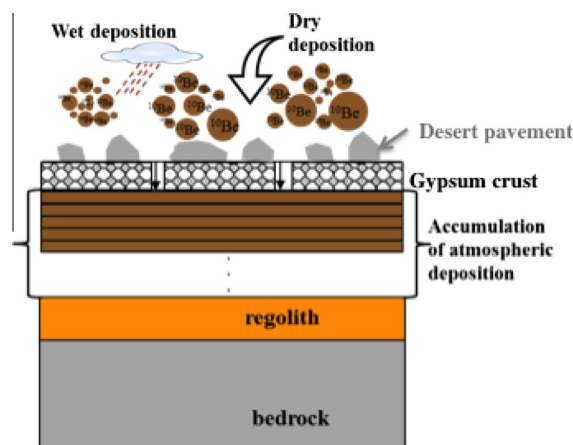

Fig. 5. The proposed layer-like soil (including ^{10}Be) accumulation mechanism.

Eq. (4) using the least-squares regression coefficients, they yield a $[^{10}Be]_i = 1.53 \pm 0.20 \times 10^8$ atoms g^{-1} and soil accumulation rate $(a) = 3.43$ $(\pm 0.22) \times 10^{-5}$ cm yr^{-1} (uncertainties arising from the regression fittings with $r^2 > 0.85$) (Fig. 4). Based on this soil accumulation rate, the soil age is estimated to be ~6.6 ± 0.4 Ma at a depth of 225 cm. The net total soil mass accumulation rate is then derived by multiplying the corresponding soil accumulation rate $(3.43 \times 10^{-5}$ cm yr$^{-1})$ and the average soil density $(1.4$ g cm$^{-3})$, yielding 4.8×10^{-5} g cm^{-2} yr^{-1}.

This accumulation rate is not out of line with other accumulation rates in arid systems. A ~60 cm soil developed on a 580 ± 160 ky old basalt flow in the Mojave Desert (Anderson et al., 2002) yields a soil mass accumulation rate of ~1.5×10^{-4} g cm^{-2} yr^{-1} (assuming a soil bulk density of ~1.5 g cm^{-3}). The study site's accumulation rate is also similar to the bulk soil accumulation rate at the Yungay site in the Atacama (Ewing et al., 2006) if it is assumed that a similar soil accumulation mechanism has occurred. Dividing Ewing et al.'s total soil mass of 1.9×10^2 g cm^{-2} (the sum of the multiplication of the bulk soil density for each layer and the soil layer depth to a depth of 1.5 m based on Table 5c in Ewing et al., 2006) by the surface exposure dating age of 2.1 Ma age gives a soil accumulation rate of ~9.3×10^{-5} g cm^{-2} yr^{-1}. Ewing et al. (2006) assumed some of the Yungay soil profile was a pre-existing alluvium, but it was indistinguishable from silicate dust because their immobile element Zr concentrations were similar. Our microscopy observations and mineralogy measurement also indicated that soil particles are similar to those found in atmospheric deposition traps, suggesting the same origin of local soils and atmospheric dust. Therefore, we propose that the soil mass change at the Yungay site is not only limited to the atmospheric salt gains as noted by Ewing et al. (2006), but should be faster than the net geological accumulation rate of 4×10^{-5} g cm^{-2} yr^{-1} (Table 4 in Ewing et al., 2006) that was inferred from the soil salt and silica inventory and estimated age. Our proposed soil formation mechanism is then not significantly different from that proposed by Ewing et al. (2006). Indeed, the evolution of an insoluble soil matrix by atmospheric deposition that "effectively raises the soil surface over time" was previously inferred (Ewing et al., 2006), but lacked a quantitative rate because of uncertainties in the silicate mineral flux.

This net soil mass accumulation rate $(4.8 \times 10^{-5}$ g cm^{-2} yr$^{-1})$ inferred from the meteoric ^{10}Be data is roughly 7–15 times lower than that estimated using the measured bulk dust flux, but this is not contradictory and can be explained by two effects. First, the soil accumulation rate is the long term net accumulation rate whereas the trap rates reflect the short term accumulation rate, somewhere between the gross and net rates. For example, the sum of dust trap salt and silica deposition rates $(4 \times 10^{-4}$ g cm^{-2} yr$^{-1})$ at Yungay site 150 km southwest of our site is also 9 times higher than the sum of soil salt and silica net geological accumulation rate $(4 \times 10^{-5}$ g cm^{-2} yr$^{-1})$ (Table 4 in Ewing et al., 2006). Second, regional mining, off-road driving, and wind erosion of disturbed surfaces (field observations) entrain large amounts of local eolian material, which enhances the modern accumulation (deposition)

relative to preindustrial times. For example, the dust flux in the modern Mojave of 13.2–14.0×10^{-4} g cm^{-2} yr^{-1} is impacted by human activity (Reheis and Kihl, 1995) and is 10 times higher than net accumulation rate of ~1.5×10^{-4} g cm^{-2} yr^{-1} on the nearby basalt flows (Anderson et al., 2002).

The modeled $[^{10}Be]_i$ value of 1.53×10^8 atoms g^{-1} is close to the $[^{10}Be]$ measured in sub-surface soils (1.36–1.45×10^8 atoms g^{-1}), but slightly higher than the $[^{10}Be]$ in atmospheric dust ($1.24 \pm 0.19 \times 10^8$ atoms g^{-1}). This also suggests that common open-pit mining in the area may have entrained older subsurface material, which would have low ^{10}Be activity, into the troposphere and it was subsequently deposited into the dust traps. Also, the rainless dust collection period may have had less ^{10}Be deposition (see paleoclimate discussion below) relative to the long term total that includes wet deposition.

Similarly, a ^{10}Be soil accumulation rate, $R[^{10}Be]_{accum}$ (atoms cm^{-2} yr^{-1}), can be approximated using soil ^{10}Be data by:

$$R[^{10}Be]_{accum} = [^{10}Be]_i \times \rho \times a \times f \qquad (5)$$

where ρ is the average soil bulk density (1.4 g cm^{-3}), and f is the average fraction of soil insoluble material (0.92). This yielded a $R[^{10}Be]_{accum}$ value of 6.8×10^3 atoms cm^{-2} yr^{-1}. The soil $R[^{10}Be]_{accum}$ is only 18% of the observed trap F_{10Be}. This difference suggests two possible scenarios. The first scenario would suggest that there was only a partial retention of the bulk ^{10}Be that was deposited, with more than 82% being lost to wind erosion. Alternatively, anthropogenic entrainment (open pit mining) of old surface material with low ^{10}Be activities was deposited into the dust traps and accounted for >82% of dust deposition. However, it is more likely that both scenarios were important, and the $R[^{10}Be]_{accum}$ represents the average net ^{10}Be accumulation rate in the soil over the past 6.6 My.

The total soil profile age of ~6.6 Ma is striking since soils in other regions rarely date older than the Pleistocene. This estimate is also 17 times the age estimate of 386 ky based on soil ^{10}Be inventory. However, as we discussed above, the ^{10}Be inventory-based age of 386 ky is not in line with other estimates in the Atacama and can only be viewed as the minimum soil age for the two following reasons. First, anthropogenic entrainment of old surface material with ^{10}Be probably led to an overestimation of soil ^{10}Be flux, and then younger soil age estimate. Second, as we mentioned above, because of its low precipitation rates, the ^{10}Be deposition should be mainly from dry deposition and accumulate in the soil layers, and therefore, which may not be leached down and fully retained as in most other regions. Therefore, there might be a far slower soil ^{10}Be accumulation than the atmospheric^{10}Be flux measured by dust traps which did not mimic the losses through wind erosion or other processes. Instead, the accumulation model estimate of 6.6 Ma is in line with other soil age constraints in the Atacama. It is similar to the age of 6.67 ± 0.13 Ma of nearby ~4 m thick coarse alluvial sediment (Placzek et al., 2009). Some stable landforms in central Atacama have younger surface exposure ages

(1.5–2.6 Ma) (Ewing et al., 2006; Placzek et al., 2010), but these differences could be due to different landform development history and dissimilar geographic conditions (e.g. exhumation, weathering or mobilization of surface clasts/boulders).

5.3. Interpretation for the accumulation model-data deviations

While there is an excellent agreement in the model-data fit, there exist some small deviations at some depths that may be meaningful (Fig. 4). The small deviations are likely due to the uncertainties in the model assumptions of (1) constant meteoric ^{10}Be production, (2) constant dust production, (3) constant ^{10}Be delivery, and (4) no post-depositional ^{10}Be movement or mixing.

The accumulation-decay model assumes meteoric ^{10}Be production is constant, but it is well established that variations in solar modulation, interplanetary magnetic field, and geomagnetic field can alter meteoric ^{10}Be production (e.g. Christl et al., 2007), thus changing $[^{10}Be]_i$ in Eq. (4) and the model's soil age estimates. Meteoric ^{10}Be production variations are caused by the fairly regular 11-year solar cycle or stochastic solar activities (Usoskin et al., 2007), which likely average out over our temporal resolution (~150 ky). Further, the long term mean interplanetary magnetic field is commonly assumed relatively constant over 10^5–10^9 yrs (e.g. Wieler et al., 2011). Therefore, only variations in ^{10}Be production induced by changes in geomagnetic intensity were modeled to explore potential impact on the $[^{10}Be]_i$ value. The global absolute paleointensity (PINT) database, which catalogues all absolute palaeointensity data with ages >50 ka (Biggin et al., 2010), was used to select high-quality virtual dipole moment (VDM) data in the past 7 Ma. The selected VDMs were averaged over 100 ky, and then used to derive dipolar latitudinal geomagnetic cutoff rigidities (Lifton et al., 2008). These rigidities and the long term average solar modulation potential (550 MV) were used to estimate the globally-averaged scaling factors for ^{10}Be production rates relative to the global mean production rate in 1950 (Kovaltsov and Usoskin, 2010). The production scaling factors were also derived from the latest PADM2M (0-2 Ma paleomagnetic axial dipole moment) model, which is based upon globally distributed paleointensity records spanning 0–2 Ma (Ziegler et al., 2011), and were compared with those from PINT database. Time-varying $[^{10}Be]_{i(t)}$ were then calculated using the production scaling factors and the model-estimated $[^{10}Be]_i$ of 1.53×10^8 atoms g^{-1} (Appendix A Tables A.1 and A.2). Each observed soil $[^{10}Be]$ value was corrected for decay to yield $[^{10}Be]_{i(h)}$ as a function of depth (h) following Eq. (4) using $a = 3.43 \times 10^{-5}$ cm yr^{-1}. Assuming temporal variations in the global mean production rate are representative of geomagnetic effects at our site, the comparison between $[^{10}Be]_{i(h)}$ and $[^{10}Be]_{i(t)}$ shows that VDM changes alter $[^{10}Be]_{i(t)}$ by less than a factor of 1.5 and are out of phase with $[^{10}Be]_{i(h)}$ variations. This indicates that the VDM variations could not account for all the significant discrepancies in $[^{10}Be]_{i(h)}$, especially around 1, 2.5, 3.5, and 5 Ma, suggesting other processes besides

geomagnetic field change were affecting $[^{10}Be]$ over time (depth) in our soils.

The accumulation-decay model estimates could also be impacted if the assumption (2), a constant atmospheric dust production rate, is violated. The Atacama dust is mainly originated from local entrainment of surface material (Tanaka and Chiba, 2006), which has likely been true for millions of years in view of the consistent sand-sized particles in the soil and can be mostly impacted by climate variations, atmospheric circulation and surface wind. However, the dust flux variations can be minor compared to the persistently large dust input rates in the Atacama region, different from in the Antarctic region where multiple-fold change in dust flux was observed maybe because the low dust flux rate was subject to disturbance. Model estimates by Mahowald et al. (1999) suggested that the Atacama region would experience from almost no change to at most a two-fold change in annual dust deposition (production) during glacial-interglacial periods. However, local dust production variations tend to average out over ~150 ky that is 5 cm sampling resolution in our profile. Additionally, an increase in the amount of atmospheric dust will lead to an increase of the soil accrual rate of dust, but probably with a minimal change to the $[^{10}Be]_i$. In Eq. (4), we can tell that the soil accrual rate change has a small influence on soil $[^{10}Be]$. Hence, regional dust production variations are not likely to have considerably impacted the model's age estimates, or to account for the deviations between the model and observations. Therefore, discrepancies between the model-predicted and observed ^{10}Be concentrations could be accounted for by inconstant ^{10}Be delivery rate and/or the post-depositional ^{10}Be movement and mixing during pedogenesis. Climate change is thus the most likely cause of the deviations between the data and the modeled $[^{10}Be]$ (Fig. 6). The climate effect would be via different ^{10}Be delivery efficiencies of different sized aerosols via dry and wet deposition or the mobilization of small particles with ^{10}Be during periods of enhanced precipitation.

An increase in wet deposition would increase ^{10}Be delivery by removing different sized aerosols with different efficiencies. Dry deposition is dominated by gravitational settling of 10–100 μm diameter particles, which account for most of the aerosol mass. The dust trap mass and grain morphology suggests that reworking of local sands and deposition of 10–100 μm diameter particle are the main contributors to deposition mass. ^{10}Be uptake, on the other hand, occurs mostly on sub-micron sized aerosols in the stratosphere where ^{10}Be is produced (Gaffney et al., 2004). This results in that large particles (>1 μm), with short residence time in the atmospheric boundary layer, have low ^{10}Be activities (Papastefanou, 2010), and their deposition may contribute a relatively stable but small amount of meteoric ^{10}Be flux to the ground via dry deposition.

In contrast, wet deposition scavenges particles of all sizes in the air column (Seinfeld and Pandis, 2006), which would include those sub-micron particles with high ^{10}Be activities. In humid regions where frequent rainfall events efficiently scavenge particulate ^{10}Be, the ^{10}Be deposition rate is likely only dependent on the abundance of meteoric
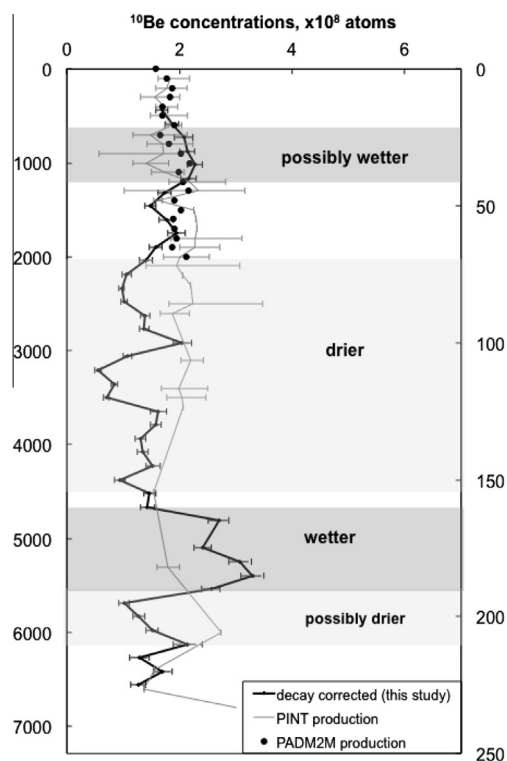
Fig. 6. Decay-corrected soil ^{10}Be concentrations ($[^{10}Be]_{i(h)}$) were compared to time-varying $[^{10}Be]_{i(t)}$ that was corrected by the PINT database-derived and PADM2M model-derived production scaling factors based on the regression-derived $[^{10}Be]_i$ of 1.53×10^8 - atoms g^{-1}. Error bars for PINT-based production reflect the scattering of data from different sources.

^{10}Be. In contrast, dry deposition and rare rainfall in the hyper-arid regions are likely unable to scavenge all the meteoric ^{10}Be in the boundary layer, resulting in significantly lower ^{10}Be deposition fluxes. This is evident at our site and the Antarctic Dry Valleys where ^{10}Be deposition is only 2–6% of the present global average (Bettoli et al., 1993; Field et al., 2006). Therefore, even a small increase in wet deposition would show a precipitation additive effect to increase ^{10}Be deposition and *vice versa* at our site, as observed in New Zealand paleosols by Graham et al. (2001) with increased ^{10}Be inputs and $^{10}Be/^9Be$ ratios during warmer, wetter interglacial times. Thus, the positive ^{10}Be excursions (Fig. 6) can be explained by an increase in precipitation, while the negative excursions suggest decreased precipitation, relative to the long term average precipitation. The minimum decay-corrected $[^{10}Be]_{i(h)}$ of 5.59×10^7 atoms g^{-1} at ~3.2 Ma may then correspond to the extremely dry conditions and represent the $[^{10}Be]_i$ in dry deposition, while the maximum decay-corrected $[^{10}Be]_{i(h)}$ of 3.30×10^8 atoms g^{-1} around 5.4 Ma may indicate the wettest climate in the past 6.6 Ma. A simple model has estimated that the degree of increased precipitation needed to produce these excursions is 2–5 times the current mean annual precipitation rate of 0.4 mm (see Appendix B).

The model-data deviations could also arise if there has been post-depositional ^{10}Be movement and mixing during pedogenesis. Large-scale ^{10}Be movement is unlikely based

on previously discussed issues of solubility. If large-scale advective, active or diffusive transport were at play then we would expect a homogenous ^{10}Be profile. Indeed, the exponential decrease in ^{10}Be is evidence that these transport mechanisms are not significant processes at this site. This is in contrast to soluble anion (Cl^-, NO_3^- and SO_4^{2-}) concentration profiles that varied with depth and had peak concentrations at ~200 cm (Fig. 3). These anions can typically form NaCl, NaNO$_3$ Na$_2$SO$_4$ and CaSO$_4$ minerals which have solubility product constants (K_{sp}) of 3.14×10^{-5}–1.12×10^3 mol^2 L^{-2} at 25 °C (Haynes, 2014). Due to their solubility properties, these minerals would be free to migrate during sporadic small water flows, yet they have only migrated 200 cm (Fig. 3). In essence, the soluble salt age between the surface and the depth of 225 cm may be significantly younger than the silicate matrix, the older salt having been leached to deeper depths. These all suggest that ^{10}Be movement was not freely available. Significant physical transport of ^{10}Be attached small grains rather than dissolution is also not supported by the grain size distribution that was relatively consistent with depth and no abrupt textural transitions were observed (Fig. 3). Even if there does exist limited movement of ^{10}Be, similar to the enhanced ^{10}Be delivery mechanism, the ^{10}Be positive excursions are probably an indication of increased precipitation that can move more ^{10}Be and *vice versa*. This minimal ^{10}Be movement would be consistent with the low ^{10}Be mobility in a New Zealand loess-paleosol profiles that are significantly wetter (annual precipitation: ~900 mm) and more acidic than our site by Graham et al. (2001). The overall limited migration behavior of ^{10}Be within the soil profile also supports our accumulation model that soil matrix including ^{10}Be is building up as layers over time, rather than that ^{10}Be is migrating through a pre-existing soil.

We suggest that the soil decay-corrected ^{10}Be profile reflects a combination of global and regional climate change, in particular modulation of the El Niño-Southern Oscillation. Our data suggest that, compared to the long term average, the Atacama's climate was wetter during intervals spanning 5.6–4.7 Ma and possibly 1.3–0.6 Ma (to a lesser degree), and drier during periods spanning between 4.5–2.0 Ma and possibly 6.3–5.6 Ma. Aridity in the hyper-arid core of the Atacama is influenced by El Niño-La Niña climate conditions. There is typically an increase in Andean snowfall and subsequent river discharge during La Niña conditions due to an increase in moisture transported from the Amazonian basin. However, the rain shadow effect of the Andean Cordillera limits the impact of this increased moisture in the Atacama's central depression, resulting in intensified acidification in the Atacama during La Niña conditions (Houston, 2006). In contrast, during El Niño climate conditions, rainfall in the Atacama's central depression is enhanced by moisture influx from the Pacific (Houston, 2006). Thus, a drier climate spanning 6.3–5.6 Ma would suggest that a more La Niña-like climate state was in place just prior to the onset of the Pliocene, and this would, however, indicate a wetter Altiplano during this period. Increased desiccation at *ca.* 6 Ma inferred from evaporite precipitation and salt crust formation in the

Atacama (Hartley and Chong, 2002) supports this hypothesis. The decay-corrected [10]Be data also suggests a permanent El Niño-like condition began around 5.6 Ma and terminated around 4.7 Ma (Fig. 6). This is consistent with semi-arid episodes during late Miocene inferred from supergene enriched alunite-group minerals in the Atacama (Bissig and Riquelme, 2010). Models and other global proxy data have also suggested a permanent El Niño-like condition prevailed during the early Pliocene ~5 Ma (Dekens et al., 2008; Bonham et al., 2009; Fedorov et al., 2013). The decay-corrected [10]Be data indicates that after the termination of the El Niño-like climate at 4.7 Ma, a La Niña-like climate arose resulting in a drier central depression, and thus a wetter Altiplano. This condition existed until roughly 2 Ma. Such a La Niña-like state occurring between 4 and 3 Ma, resulting in an estimated fourfold increase in heavy storm events in the Altiplano, has recently been proposed based on enhanced Andean incision rates by Lease and Ehlers (2013). During the dry period 4.5–2.0 Ma, the decay-corrected [10]Be data also exhibits a distinct positive excursion occurring between 3.2 and 2.5 Ma, which we interpret as a small and brief increase in central depression rainfall compared to the surrounding dry periods. This corresponds well with proxy analysis and paleoclimate models that suggest a middle Pliocene warm period occurred ~3 Ma (Haywood et al., 2009; Williams et al., 2009). In the upper section of the profile, a brief less arid period is inferred at ~1 Ma, prior to enhanced desiccation in the Pleistocene, which concurs with a recent surface erosion study that showed wetter climates in the Atacama during the last 1 Ma as well as 5.5–4.5 Ma by Jordan et al. (2014). However, two other wetter periods between 4–3.6 Ma and 2.6–2.2 Ma suggested by Jordan et al. (2014) do not appear but are probably incorporated into our lengthy dry period in our [10]Be profile. Also it must be acknowledged that there are some uncertainties associated with these interpretations. At the current sampling resolution and detection limits, the [10]Be proxy resolution is not sufficient for detecting precipitation changes that might be associated with Pleistocene glacial-interglacial cycles in the upper section of the profile. Also, the conclusion of a drier period during 6.3–5.7 Ma is tentative because of the lack of extensive paleointensity data at ~6 Ma.

6. CONCLUSIONS

Meteoric [10]Be dating has proved successful in establishing a depth-dependent soil chronology, providing perspectives on soil formation mechanism, and paleoclimate change over the past millions of years in the hyper-arid Atacama. An exponential decrease of soil [10]Be concentrations with depth was well reproduced by a simple accumulation-decay model that soil matrix, including [10]Be, builds up as layers over time while [10]Be decays *in situ*, suggesting the soil is primarily formed by the slow accumulation of atmospheric dust. The model-estimated soil age of ~6.6 Ma at 225 cm is comparable with soil age estimates at several other sites in the Atacama. Changes in paleo-precipitation may account for the model-data misfit, suggesting wetter climates during the intervals of 5.6–4.7 Ma and

possibly 1.3–0.6 Ma, and drier climates during 4.5–2.0 Ma and possibly 6.3–5.6 Ma, compared to the long term average. The changes in local precipitation inferred from the data are linked to oscillations between long term El Niño-(wetter Atacama) and La Niña (drier Atacama)-like climate states.

APPENDIX A.

APPENDIX B. PALEO-PRECIPITATION ESTIMATION

Paleo-precipitation during the wettest period around 5.4 Ma can be roughly inferred based on some assumptions and calculations. The scheme is to estimate (1) the large (>1 μm) and small (<1 μm) aerosol dry deposition rates, (2) the large and small aerosol wet deposition rates, (3) the ratios of [10]Be flux during wet relative to dry periods, and (4) the historic precipitation amounts. Firstly, the large to small aerosol mass concentrations are assumed to be 3.5×10^{-12} g cm^{-3} and 1.5×10^{-12} g cm^{-3}, respectively, which are based on the median values for aerosols in remote continents from Seinfeld and Pandis (2006). Assuming all particles are spheres, the average gravitational settling velocities for the large to small aerosols can be calculated using:

$$v_s = D_p^2 \rho_p g C_c / (18\mu) \tag{B.1}$$

where D_p is the particle diameter (1×10^{-4} cm and 1×10^{-5} cm for large and small particles, respectively), ρ_p is the particle density (2.6 g cm^{-3} for typical desert dust particles from Nickovic et al. (2001)), g is the gravitational acceleration (9.8 m s^{-2}), C_c is the slip correction factor (Cunninghan correction factor) of 1.08 and 2.86 for large and small particles, respectively (calculated based on the equation $C_c = 1 + 2\lambda/d_p[1.257 + 0.4\exp(-1.1d_p/2\lambda)]$, where λ is the mean free path of gas molecules in air of 0.065×10^{-6} m), and μ is air dynamic viscosity of 1.8×10^{-2} g m^{-1} s^{-1} (Seinfeld and Pandis, 2006). This gives the large and small aerosol gravitational settling velocities of 9.4×10^{-3} and 2.3×10^{-4} cm s^{-1}, respectively. The dry flux of large and small particles to the ground would be the product of the gravitational settling velocity and the aerosol mass concentrations, giving the dry deposition rates

Table A.1
Production rates derived from PINT paleointensity variations.

Age_ka	VDM_avg[b] ($\times$E+22)	VDM_std	VDM_n	VDM/M$_{1950}$	Production rate[d], atoms s^{-1} cm^{-2}	Production scaling factor	[Be]$_{i(t)}$
1950[a]	8.0648[c]			1.00	3.05E−02	1.00	1.53E+08[e]
100	5.7062	3.39	21	0.71	3.66E−02	1.20	1.83E+08
200	6.0573	2.16	32	0.75	3.54E−02	1.16	1.78E+08
300	7.7666	2.94	15	0.96	3.11E−02	1.02	1.56E+08
400	6.3406	2.72	5	0.79	3.46E−02	1.13	1.73E+08
500	6.3746	1.66	15	0.79	3.45E−02	1.13	1.73E+08
600	5.5026	2.22	9	0.68	3.73E−02	1.22	1.87E+08
700	8.6144	1.92	5	1.07	2.94E−02	0.96	1.48E+08
800	6.6481	3.75	29	0.82	3.37E−02	1.11	1.69E+08
900	6.4647	3.22	13	0.80	3.42E−02	1.12	1.72E+08
1000	9.4145	3.64	12	1.17	2.80E−02	0.92	1.41E+08
1100	6.2702	2.48	2	0.78	3.48E−02	1.14	1.74E+08
1200	4.0317	1.40	3	0.50	4.34E−02	1.42	2.18E+08
1300	3.4746	2.03	2	0.43	4.64E−02	1.52	2.33E+08
1400	7.2412	4.72	2	0.90	3.23E−02	1.06	1.62E+08
1500	3.7411	0.34	2	0.46	4.49E−02	1.47	2.25E+08
1600	3.6075	0.00	1	0.45	4.56E−02	1.50	2.29E+08
1700	3.5397	0.00	1	0.44	4.60E−02	1.51	2.31E+08
1800	3.6231	0.00	1	0.45	4.55E−02	1.49	2.28E+08
1900	3.6372	2.62	2	0.45	4.55E−02	1.49	2.28E+08
2000	4.7743	1.98	5	0.59	4.01E−02	1.31	2.01E+08
2100	5.0997	2.43	31	0.63	3.88E−02	1.27	1.95E+08
2200	4.5689	4.99	2	0.57	4.10E−02	1.34	2.06E+08
2300	3.9656	0.00	1	0.49	4.38E−02	1.43	2.20E+08
2500	3.7850	0.00	1	0.47	4.47E−02	1.47	2.24E+08
2600	5.4875	4.79	8	0.68	3.73E−02	1.22	1.87E+08
3100	3.9444	1.23	5	0.49	4.39E−02	1.44	2.20E+08
3400	4.9405	1.20	2	0.61	3.94E−02	1.29	1.98E+08
3500	4.5990	2.19	2	0.57	4.08E−02	1.34	2.05E+08
3600	4.5400	1.86	15	0.56	4.11E−02	1.35	2.06E+08
4000	11.1200	1.99	10	1.38			
4500	7.9397	0.00	1	0.98	3.07E−02	1.01	1.54E+08
5300	6.0006	0.00	1	0.74	3.56E−02	1.17	1.78E+08
6000	2.3038	0.60	12	0.29	5.45E−02	1.79	2.73E+08
6400	7.8000	0.00	1	0.97	3.10E−02	1.02	1.56E+08
6600	9.9000	0.00	1	1.23	2.73E−02	0.89	1.37E+08
6800	1.6820	0.03	2	0.21	6.00E−02	1.97	3.01E+08
6900	11.5401	1.61	2	1.43			

[a] The year of 1950.

[b] VDM (virtual dipole moment) from the global absolute paleointensity (PINT) database (Biggin et al., 2010) were averaged over 100 ky intervals. To select high-quality data, the PINT database was trimmed by: (1) removing all data during polarity transitions because of the likelihood of abnormal low fields associated with transitions; (2) removing all data with a standard deviation $\geq$ 25%; (3) extracting all data using the latest Thellier or Microwave technique with pTRM checks with replicates $\geq$ 3.

[c] Dipole field of moment in 1950 (IGRF-10, http://www.ngdc.noaa.gov/IAGA/vmod/igrf.html).

[d] Interpolation between a set of pre-computed production as a grid of geomagnetic cutoff rigidity and the solar modulation potential by Kovaltsov and Usoskin (2010).

[e] The regression-derived long term average [^{10}Be]$_i$ of 1.53×10^8 atoms g^{-1}.

of 3.3×10^{-14} g cm^{-2} s^{-1} and 3.4×10^{-16} g cm^{-2} s^{-1} for large and small particles, respectively.

Secondly, assuming that an air column is 3,000 m high, the large and small aerosol amounts are 1.0×10^{-6} g cm^{-2} and 4.5×10^{-7} g m^{-2}, respectively. The aerosol wet removal efficiencies for large and small aerosols are assumed to be 0.6 and 0.5, respectively for <2 cm rainfall events or be the same of 0.8 for $\geq$2 cm rainfall events (Radke et al., 1980; Schumann, 1991). Then, for a <2 cm rainfall event, the large and small aerosol wet deposition rates can then be 6.3×10^{-7} g cm^{-2} and 2.2×10^{-7} g cm^{-2},

respectively, whereas for a >2 cm rainfall event, the large and small aerosol wet deposition rates would be 8.4×10^{-7} g cm^{-2} and 3.6×10^{-7} g cm^{-2}, respectively.

Thirdly, assuming the modern rainfall regime of one 0.5 cm rainfall event per decade, 2 cm rainfall event per century and 5 cm rainfall event per millennium (the rainfall intensity for each event is half of that in the rainfall regime adopted by Ewing et al., 2008b), there would be 15,000 <2 cm rainfall events and 1,500 rainfall events ($\geq$2 cm) over the 150 ky timescale (corresponding to 5 cm accumulation based on the previously derived accumulation rate).

Table A.2
Production rates derived from paleointensity variations.

Age_ka	PADM_avg[a] ($\times$E+22)	VDM/M$_{1950}$	Production rate, atoms s^{-1} cm^{-2}	Production scaling factor	[Be]$_{i(t)}$
1950	8.0648	1.00	3.05E−02	1.00	1.53E+08
0.0	7.5567	0.94	3.16E−02	1.03	1.58E+08
0.1	6.0292	0.75	3.54E−02	1.16	1.78E+08
0.2	5.4840	0.68	3.74E−02	1.23	1.87E+08
0.3	5.7657	0.71	3.63E−02	1.19	1.82E+08
0.4	6.5812	0.82	3.39E−02	1.11	1.70E+08
0.5	6.6342	0.82	3.38E−02	1.11	1.70E+08
0.6	5.3037	0.66	3.80E−02	1.25	1.91E+08
0.7	6.9906	0.87	3.29E−02	1.08	1.65E+08
0.8	5.8090	0.72	3.62E−02	1.19	1.82E+08
0.9	4.7095	0.58	4.05E−02	1.33	2.03E+08
1.0	3.9786	0.49	4.36E−02	1.43	2.19E+08
1.1	4.9176	0.61	3.95E−02	1.30	1.98E+08
1.2	4.5075	0.56	4.13E−02	1.35	2.07E+08
1.3	4.1304	0.51	4.31E−02	1.41	2.16E+08
1.4	5.2896	0.66	3.81E−02	1.25	1.91E+08
1.5	4.6958	0.58	4.04E−02	1.32	2.03E+08
1.6	5.4476	0.68	3.75E−02	1.23	1.88E+08
1.7	5.2684	0.65	3.82E−02	1.25	1.91E+08
1.8	5.0455	0.63	3.90E−02	1.28	1.96E+08
1.9	5.5209	0.68	3.73E−02	1.22	1.87E+08
2.0	4.3018	0.53	4.21E−02	1.38	2.11E+08

[a] PADM from the PADM2M (0–2 Ma palaeomagnetic axial dipole moment) model (Ziegler et al., 2011) were averaged over 100 ky intervals.

The dry to wet mass deposition rate ratio over 150 ky would be 10.6, and the dry deposition is accounting for 91% of the bulk deposition. Based on the ^{10}Be activity in a small particle to a large particle of 70 (Gaffney et al., 2004), the ratio of ^{10}Be via modern wet and dry deposition to ^{10}Be only via only dry deposition of 2.1, similar to the ratio of 2.2 of the measured [^{10}Be] in the dust of 1.24×10^8 atoms g^{-1} to the lowest decay-corrected [Be]$_{i(h)}$ of 5.59×10^7 atoms g^{-1}.

Finally, assuming that 5.59×10^7 atoms represent only dry deposition, our regression-derived [Be]$_i$ of 1.53×10^8 atoms g^{-1} corresponding to long term average climate and the decay-corrected [Be]$_{i(h)}$ maximum of 3.30×10^8 atoms g^{-1} corresponding to wettest climate, the long term average precipitation can be reversely estimated to be 1.6 times the modern-time precipitation, while the wettest period may have 4.6 times the number of modern-time wet events. Meanwhile, the climatic shift can also affect the dust deposition. Based on the calculation above, the dust flux may vary only by ~20% from 5 to 6 Ma wet period to modern hyper-arid period.

REFERENCES

Amit R., Enzel Y., Grodek T., Crouvi O., Porat N. and Ayalon A. (2010) The role of rare rainstorms in the formation of calcic soil horizons on alluvial surfaces in extreme deserts. *Quat. Res.* **74**, 177–187.

Amundson R., Ewing S., Dietrich W., Sutter B., Owen J., Chadwick O., Nishiizumi K., Walvoord M. and McKay C. (2008) On the *in situ* aqueous alteration of soils on Mars. *Geochim. Cosmochim. Acta* **72**, 3845–3864.

Amundson R., Dietrich W., Bellugi D., Ewing S., Nishiizumi K., Chong G., Owen J., Finkel R., Heimsath A., Stewart B. and Caffee M. (2012) Geomorphologic evidence for the late Pliocene onset of hyperaridity in the Atacama Desert. *Geol. Soc. Am. Bull.* **124**, 1048–1070.

Anderson K., Wells S. and Graham R. (2002) Pedogenesis of vesicular horizons, Cima volcanic field, Mojave Desert, California. *Soil Sci. Soc. Am. J.* **66**, 878–887.

Arthur M., Brysk H., Paveri-Fontana S. and Zweifel P. (1981) The law of radioactive decay. *II Nuovo Cimento B* **63**, 565–587.

Azua-Bustos A., Urrejola C. and Vicuña R. (2012) Life at the dry edge: Microorganisms of the Atacama Desert. *FEBS Lett.* **586**, 2939–2945.

Balistrieri L. S. and Murray J. W. (1986) The surface chemistry of sediments from the Panama Basin: the influence of Mn oxides on metal adsorption. *Geochim. Cosmochim. Acta* **50**, 2235–2243.

Bao H., Jenkins K. A., Khachaturyan M. and Díaz G. C. (2004) Different sulfate sources and their post-depositional migration in Atacama soils. *Earth Planet. Sci. Lett.* **224**, 577–587.

Betancourt J. L., Latorre C., Rech J. A., Quade J. and Rylander K. A. (2000) A 22,000-year record of monsoonal precipitation from Northern Chile's Atacama Desert. *Science* **289**, 1542–1546.

Bettoli M. G., Cantelli L., Tositti L., Tubertini O. and Valcher S. (1993) Activity of Be-7 and Pb-210 in snow samples at Terra Nova Bay–Antarctica: preliminary results. In *Environmental Radioactivity in the Arctic and Antarctic* (eds. P. Strand and E. Holm). Scientific Committee of the Environmental Radioactivity in the Arctic and Antarctic, Osteras, Norway, pp. 229–232.

Biggin A., McCormack A. and Roberts A. (2010) Palaeointensity database updated and upgraded. *EOS Trans. Am. Geophys. Union* **91**, 15.

Bissig T. and Riquelme R. (2010) Andean uplift and climate evolution in the southern Atacama Desert deduced from

geomorphology and supergene alunite-group minerals. *Earth Planet. Sci. Lett.* **299**, 447–457.

Böhlke J. K., Ericksen G. E. and Revesz K. (1997) Stable isotope evidence for an atmospheric origin of desert nitrate deposits in northern Chile and southern California, USA. *Chem. Geol.* **136**, 135–152.

Bonham S. G., Haywood A. M., Lunt D. J., Collins M. and Salzmann U. (2009) El Niño-Southern Oscillation, Pliocene climate and equifinality. *Philos. T. R. Soc. A* **367**, 127–156.

Brown E. T., Edmond J. M., Raisbeck G. M., Bourlès D., Yiou F. and Measures C. (1992) Beryllium isotope geochemistry in tropical river basins. *Geochim. Cosmochim. Acta* **56**, 1607–1624.

Chadwick O. A., Brimhall G. H. and Hendricks D. M. (1990) From a black to a gray box—A mass balance interpretation of pedogenesis. *Geomorphology* **3**, 369–390.

Chmeleff J., von Blanckenburg F., Kossert K. and Jakob D. (2010) Determination of the ^{1010}Be half-life by multicollector ICP-MS and liquid scintillation counting. *Nucl. Instrum. Methods Phys. Res. B* **268**, 192–199.

Christl M., Mangini A. and Kubik P. (2007) Highly resolved Beryllium-10 record from ODP Site 1089—A global signal? *Earth Planet. Sci. Lett.* **257**, 245–258.

Clement A. C., Cane M. A. and Seager R. (2001) An orbitally driven tropical source for abrupt climate change. *J. Clim.* **14**, 2369–2375.

Cooke R. U. (1981) Salt weathering in deserts. *P. Geologist. Assoc.* **92**, 1–16.

Covey C., AchutaRao K. M., Cubasch U., Jones P., Lambert S. J., Mann M. E., Phillips T. J. and Taylor K. E. (2003) An overview of results from the Coupled Model Intercomparison Project. *Global Planet. Change* **37**, 103–133.

Dekens P. S., Ravelo A. C., McCarthy M. D. and Edwards C. A. (2008) A 5 million year comparison of Mg/Ca and alkenone paleothermometers. *Geochem. Geophys. Geosyst.* **9**(10).

DGA (the Dirección General de Aguas) (2011) Informe Hidrológico Proyecto Antakena: http://seia.sea.gob.cl/ (accessed June 2012) (in spanish).

Ericksen G. E. (1983) The Chilean nitrate deposits. *Am. Sci.* **71**, 366–374.

Ewing S., Sutter B., Owen J., Nishiizumi K., Sharp W., Cliff S., Perry K., Dietrich W., McKay C. and Amundson R. (2006) A threshold in soil formation at Earth's arid-hyperarid transition. *Geochim. Cosmochim. Acta* **70**, 5293–5322.

Ewing S., Michalski G., Thiemens M., Quinn R., Macalady J., Kohl S., Wankel S., Kendall C., McKay C. and Amundson R. (2007) Rainfall limit of the N cycle on Earth. *Global Biogeochem. Cy.* 21, GB3009.

Ewing S. A., Macalady J. L., Warren-Rhodes K., McKay C. P. and Amundson R. (2008a) Changes in the soil C cycle at the arid-hyperarid transition in the Atacama Desert. *J. Geophys. Res.* **113**, G02S90.

Ewing S. A., Yang W., DePaolo D. J., Michalski G., Kendall C., Stewart B. W., Thiemens M. and Amundson R. (2008b) Non-biological fractionation of stable Ca isotopes in soils of the Atacama Desert, Chile. *Geochim. Cosmochim. Acta* **72**, 1096–1110.

Fedorov A. V., Brierley C. M., Lawrence K. T., Liu Z., Dekens P. S. and Ravelo A. C. (2013) Patterns and mechanisms of early Pliocene warmth. *Nature* **496**, 43–49.

Field C. V., Schmidt G. A., Koch D. and Salyk C. (2006) Modeling production and climate-related impacts on ^{10}Be concentration in ice cores. *J. Geophys. Res.* **111**, D15107.

Gaffney J. S., Marley N. A. and Cunningham M. M. (2004) Natural radionuclides in fine aerosols in the Pittsburgh area. *Atmos. Environ.* **38**, 3191–3200.

Garreaud R., Vuille M. and Clement A. C. (2003) The climate of the Altiplano: observed current conditions and mechanisms of past changes. *Palaeogeogr. Palaeoclimatol. Palaeoecol.* **194**, 5–22.

Gayo E. M., Latorre C., Jordan T. E., Nester P. L., Estay S. A., Ojeda K. F. and Santoro C. M. (2012) Late Quaternary hydrological and ecological changes in the hyperarid core of the northern Atacama Desert (~21°S). *Earth-Sci. Rev.* **113**, 120–140.

Gosse J. C. and Phillips F. M. (2001) Terrestrial in situ cosmogenic nuclides: theory and application. *Quat. Sci. Rev.* **20**, 1475–1560.

Goudie A. S., Wright E. and Viles H. A. (2002) The roles of salt (sodium nitrate) and fog in weathering: A laboratory simulation of conditions in the northern Atacama Desert, Chile. *Catena* **48**, 255–266.

Graham I., Ditchburn R. and Whitehead N. (2001) Be isotope analysis of a 0–500ka loess–paleosol sequence from Rangitatau East, New Zealand. *Quat. Int.* **76**, 29–42.

Graly J. A., Bierman P. R., Reusser L. J. and Pavich M. J. (2010) Meteoric Be-10 in soil profiles – A global meta-analysis. *Geochim. Cosmochim. Acta* **74**, 6814–6829.

Granger D. E., Fabel D. and Palmer A. N. (2001) Pliocene−Pleistocene incision of the Green River, Kentucky, determined from radioactive decay of cosmogenic ^{26}Al and ^{10}Be in Mammoth Cave sediments. *Geol. Soc. Am. Bull.* **7**, 825–836.

Gu Z. Y., Lal D., Liu T. S., Southon J., Caffee M. W., Guo Z. T. and Chen M. Y. (1996) Five million year ^{10}Be record in Chinese loess and red-clay: climate and weathering relationships. *Earth Planet. Sci. Lett.* **144**, 273–287.

Hartley A. and Chong G. (2002) Late Pliocene age for the Atacama Desert: implications for the desertification of western South America. *Geology* **30**, 43–46.

Haug E. W., Kraal E. R., Sewall J. O., Van Dijk M. and Diaz G. C. (2010) Climatic and geomorphic interactions on alluvial fans in the Atacama Desert, Chile. *Geomorphology* **121**, 184–196.

Haynes, W. M. (ed.) (2014) *CRC handbook of chemistry and physics*. CRC Press, Boca Raton.

Haywood A. M., Dowsett H. J., Valdes P. J., Lunt D. J., Francis J. E. and Sellwood B. W. (2009) Introduction. Pliocene climate, processes and problems. *Philos. T. R. Soc. A* **367**, 3–17.

Heikkilä U. (2007) *Modeling of the atmospheric transport of the cosmogenic radionuclides ^{10}Be and ^{7}Be using the ECHAM5-HAM General Circulation Model* Ph.D. thesis. ETH-Zurich.

Heikkilä U. and Smith A. (2013) Production rate and climate influences on the variability of 10Be deposition simulated by ECHAM5-HAM: Globally, in Greenland, and in Antarctica. *J. Geophys. Res.* **118**, 2506–2520.

Hewitson B. and Crane R. (2006) Consensus between GCM climate change projections with empirical downscaling: precipitation downscaling over South Africa. *Int. J. Climatol.* **26**, 1315–1337.

Houston J. (2006) Variability of precipitation in the Atacama Desert: its causes and hydrological impact. *Int. J. Climatol.* **26**, 2181–2198.

Houston J. and Hartley A. J. (2003) The central Andean west-slope rainshadow and its potential contribution to the origin of hyper-aridity in the Atacama Desert. *Int. J. Climatol.* **23**, 1453–1464.

Hulme M., Doherty R., Ngara T., New M. and Lister D. (2001) African climate change: 1900–2100. *Clim. Res.* **17**, 145–168.

Jenny H. (1941) *Factors of soil formation: a system of quantitative pedology*. McGraw-Hill Book Company, New York.

Jordan T. E., Kirk-Lawlor N. E., Blanco N., Rech J. A. and Cosentino N. J. (2014) Landscape modification in response to repeated onset of hyperarid paleoclimate states since 14 Ma, Atacama Desert, Chile. *Geol. Soc. Am. Bull.* **126**, 1016–1046.

Joubert A. and Hewitson B. (1997) Simulating present and future climates of southern Africa using general circulation models. *Prog. Phys. Geogr.* **21**, 51–78.

Jungers M. C., Heimsath A. M., Amundson R., Balco G., Shuster D. and Chong G. (2013) Active erosion–deposition cycles in the hyperarid Atacama Desert of Northern Chile. *Earth Planet. Sci. Lett.* **371**, 125–133.

Kovaltsov G. A. and Usoskin I. G. (2010) A new 3D numerical model of cosmogenic nuclide ^{10}Be production in the atmosphere. *Earth Planet. Sci. Lett.* **291**, 182–188.

Lal D. (1987) ^{10}Be in polar ice. Data reflect changes in cosmic ray flux or polar meteorology. *Geophys. Res. Lett.* **14**, 785–788.

Lease R. O. and Ehlers T. A. (2013) Incision into the Eastern Andean plateau during Pliocene cooling. *Science* **341**, 774–776.

Li Y. H., Burkhardt L., Buchholtz M., O'Hara P. and Santschi P. (1984) Partition of radio tracers between suspended particles and seawater. *Geochim. Cosmochim. Acta* **48**, 2011–2019.

Lifton N., Smar D. and Shea M. (2008) Scaling time-integrated in situ cosmogenic nuclide production rates using a continuous geomagnetic model. *Earth Planet. Sci. Lett.* **268**, 190–201.

Mahowald N., Kohfeld K., Hansson M., Balkanski Y., Harrison S. P., Prentice I. C., Schulz M. and Rodhe H. (1999) Dust sources and deposition during the last glacial maximum and current climate: A comparison of model results with paleodata from ice cores and marine sediments. *J. Geophys. Res.* **104**, 15895–15916.

Masarik J. and Beer J. (2009) An updated simulation of particle fluxes and cosmogenic nuclide production in the Earth's atmosphere. *J. Geophys. Res.* **114**, D11103.

McFadden L. D., Wells S. G. and Jercinovich M. J. (1987) Influences of eolian and pedogenic processes on the origin and evolution of desert pavements. *Geology* **15**, 504–508.

Michalski G., Böhlke J. and Thiemens M. (2004) Long term atmospheric deposition as the source of nitrate and other salts in the Atacama Desert, Chile: new evidence from mass-independent oxygen isotopic compositions. *Geochim. Cosmochim. Acta* **68**, 4023–4038.

Moreno T. and Gibbons W. (2007) *The Geology of Chile*. The Geological Society Publishing House, London, UK.

Nickovic S., Kallos G., Papadopoulos A. and Kakaliagou O. (2001) A model for prediction of desert dust cycle in the atmosphere. *J. Geophys. Res.* **106**(18113–18118), 18129.

Nishiizumi K., Imamura M., Caffee M. W., Southon J. R., Finkel R. C. and McAninch J. (2007) Absolute calibration of ^{10}Be AMS standards. *Nucl. Instrum. Methods Phys. Res. B* **258**, 403–413.

Owen J. J., Amundson R., Dietrich W. E., Nishiizumi K., Sutter B. and Chong G. (2011) The sensitivity of hillslope bedrock erosion to precipitation. *Earth Surf. Proc. Land.* **36**, 117–135.

Papastefanou C. (2010) Paths of air pollutants containing radioactive nuclides in the suburban area of Thessaloniki, Northern Greece. *Aerosol Air Qual. Res.* **10**, 354–359.

Pavich M. J. and Vidic N. (1993) Application of paleomagnetic and ^{10}Be analyses to chronostratigraphy of alpine glacio–fluvial terraces, Sava River Valley, Slovenia. *Geophys. Monogr.* **78**, 263–275.

Placzek C., Quade J., Rech J. A., Patchett P. and Pérez de Arce C. (2009) Geochemistry, chronology and stratigraphy of Neogene tuffs of the Central Andean region. *Quat. Geochron.* **4**, 22–36.

Placzek C., Matmon A., Granger D., Quade J. and Niedermann S. (2010) Evidence for active landscape evolution in the hyperarid Atacama from multiple terrestrial cosmogenic nuclides. *Earth Planet. Sci. Lett.* **295**, 12–20.

Radke L. F., Hobbs P. V. and Eltgroth M. W. (1980) Scavenging of aerosol particles by precipitation. *J. Appl. Meteorol.* **19**, 715–722.

Rech J. A., Currie B. S., Michalski G. and Cowan A. M. (2006) Neogene climate change and uplift in the Atacama Desert, Chile. *Geology* **34**, 761–764.

Reheis M. C. and Kihl R. (1995) Dust deposition in southern Nevada and California, 1984–1989: relations to climate, source area, and source lithology. *J. Geophys. Res.* **100**, 8893–8918.

Samson E., Marchand J. and Snyder K. A. (2003) Calculation of ionic diffusion coefficients on the basis of migration test results. *Mater. Struct.* **36**, 156–165.

Schumann T. (1991) Aerosol and hydrometeor concentrations and their chemical composition during winter precipitation along a mountain slope-III. Size-differentiated in-cloud scavenging efficiencies. *Atmos. Environ. A.* **25**, 809–824.

Seinfeld J. H. and Pandis S. N. (2006) *Atmospheric Chemistry and Physics: From air Pollution to Climate Change.* John Wiley & Sons, New York.

SERNAGEOMIN (2003) Mapa Geológico de Chile: versión digital. Servicio Nacional de Geologíay Minería, Publicación Geológica Digital, No. 4 (CD-ROM, versión1.0, 2003). Santiago.

Tanaka T. Y. and Chiba M. (2006) A numerical study of the contributions of dust source regions to the global dust budget. *Global Planet. Change* **52**, 88–104.

Usoskin I. G., Solanki S. K. and Kovaltsov G. A. (2007) Grand minima and maxima of solar activity: new observational constraints. *Astron. Astrophys.* **471**, 301–309.

Vargas G., Ortlieb L. and Rutllant J. (2000) Aluviones históricos en Antofagasta y su relación con eventos El Niño/Oscilación del Sur. *Revista Geológica de Chile* **27**, 157–176.

Wang F. (2013) *The Mechanism and Timescales of Soil Formation in the Hyper-arid Atacama Desert, Chile* Ph D thesis. Purdue University.

Wang F., Michalski G., Seo J. H. and Ge W. S. (2014) Geochemical, isotopic, and mineralogical constraints on atmospheric deposition in the hyper-arid Atacama Desert, Chile. *Geochim. Cosmochim. Acta* **135**, 29–48.

Warren-Rhodes K., Rhodes K., Pointing S., Ewing S., Lacap D., Gómez-Silva B., Amundson R., Friedmann E. and McKay C. (2006) Hypolithic cyanobacteria, dry limit of photosynthesis, and microbial ecology in the hyperarid Atacama Desert. *Microb. Ecol.* **52**, 389–398.

Wieler R., Beer J. and Leya I. (2011) The galactic cosmic ray intensity over the past 10^6–10^9 years as recorded by cosmogenic nuclides in meteorites and terrestrial samples. *Space Sci. Rev.*. http://dx.doi.org/10.1007/s11214-011-9769-9.

Willenbring J. K. and von Blanckenburg F. (2010) Meteoric cosmogenic Beryllium-10 adsorbed to river sediment and soil: applications for Earth-surface dynamics. *Earth Sci. Rev.* **98**, 105–122.

Williams M., Haywood A. M., Harper E. M., Johnson A. L., Knowles T., Leng M. J., Lunt D. J., Okamura B., Taylor P. D. and Zalasiewicz J. (2009) Pliocene climate and seasonality in North Atlantic shelf seas. *Philos. T. R. Soc. A* **367**, 85–108.

You C. F., Lee T. and Li Y. H. (1989) The partition of Be between soil and water. *Chem. Geol.* **77**, 105–118.

Ziegler L., Constable C., Johnson C. and Tauxe L. (2011) PADM2M: a penalized maximum likelihood model of the 0–2 Ma palaeomagnetic axial dipole moment. *Geophys. J. Int.* **184**, 1069–1089.

Associate editor: Anthony Dosseto